SPONSORED BY R&D SYSTEMS INC.

NEW! INTERACTIVE Pathways & Processes
Start Exploring Now
R&D SYSTEMS
www.rndsystems.com/pathways

Integrated Compact Optical Vortex Beam Emitters

Xinlun Cai *et al.*

Science **338**, 363 (2012);
DOI: 10.1126/science.1226528

This copy is for your personal, non-commercial use only.

If you wish to distribute this article to others, you can order high-quality copies for your colleagues, clients, or customers by clicking here.

Permission to republish or repurpose articles or portions of articles can be obtained by following the guidelines here.

The following resources related to this article are available online at www.sciencemag.org (this information is current as of October 18, 2012):

Updated information and services, including high-resolution figures, can be found in the online version of this article at:
http://www.sciencemag.org/content/338/6105/363.full.html

Supporting Online Material can be found at:
http://www.sciencemag.org/content/suppl/2012/10/17/338.6105.363.DC1.html
http://www.sciencemag.org/content/suppl/2012/10/17/338.6105.363.DC2.html

A list of selected additional articles on the Science Web sites **related to this article** can be found at:
http://www.sciencemag.org/content/338/6105/363.full.html#related

This article **cites 29 articles**, 1 of which can be accessed free:
http://www.sciencemag.org/content/338/6105/363.full.html#ref-list-1

Downloaded from www.sciencemag.org on October 18, 2012

Science (print ISSN 0036-8075; online ISSN 1095-9203) is published weekly, except the last week in December, by the American Association for the Advancement of Science, 1200 New York Avenue NW, Washington, DC 20005. Copyright 2012 by the American Association for the Advancement of Science; all rights reserved. The title *Science* is a registered trademark of AAAS.

leading to the formation of single-domain, elongated needle-like superparticles with $l = 11 \pm 4$ µm and $d = 1.1 \pm 0.3$ µm (Fig. 4, B and C). These single-domain superparticles have a different morphology from those multidomain superparticles made from identical nanorods without incubation treatment (fig. S21, C to E).

The needle-like superparticles from unoptimized syntheses exhibit a PL quantum yield of ~40% and are indefinitely stable in solvents with strong polarity, such as water or ethanol. However, these particles can undergo intraparticle ripening in lower-polarity solvents such as ethylene glycol, demonstrating that the needle-like morphology is not an equilibrium shape (fig. S23). The mesoscopic sizes of these needle-like superparticles allow them to be easily aligned into unidirectional line patterns on Si_3N_4 substrates through capillary forces (*24*) (fig. S24), which can be readily transferred into uniform and removable thin films of polydimethylsiloxane (PDMS) with sizes as large as 5.0 cm × 5.0 cm (Fig. 4, D and E, and fig. S25). The resulting thin films exhibit strong linearly polarized PL at 579 nm with a typical emission polarization ratio [$\rho = (I_{\parallel} - I_{\perp})/(I_{\parallel} + I_{\perp})$, where $I_{\parallel}$ and $I_{\perp}$ are the intensities parallel ($I_{\parallel}$) and perpendicular ($I_{\perp}$) to the nanorod long axis] of 0.88 (Fig. 4F and fig. S26), which is substantially higher than that of individual single CdSe-CdS nanorods [0.75 (*25*, *26*)]. This PL anisotropy enhancement can be attributed to a combination of dielectric effect and collective electric dipole coupling effects among the CdSe-CdS nanorods inside the elongated needle-like superparticles embedded in PDMS films (*26*–*28*). In addition, we show that the superparticle-embedded PDMS films can be used as energy downconversion phosphors to build polarized light-emitting diodes (Fig. 4, G to J, and fig. S27).

Our results show that anisotropic interactions of CdSe-CdS nanorods can be used to synthesize colloidal superparticles with multiple well-defined supercrystalline domains under thermodynamic equilibrium. Functionality-based anisotropic interactions between these nanorods can be kinetically introduced during the superparticle synthesis, leading to the formation of single-domain, needle-like particles. We anticipate that these findings can be extended for the self-assembly of nano-objects having other anisotropic shapes, as well as the self-assembly of two or more types of anisotropic nano-objects into well-defined mesoscopic and macroscopic complex architectures (*1*–*3*).

References and Notes

1. G. M. Whitesides, B. Grzybowski, *Science* **295**, 2418 (2002).
2. S. Mann, *Nat. Mater.* **8**, 781 (2009).
3. S. C. Glotzer, M. J. Solomon, *Nat. Mater.* **6**, 557 (2007).
4. M. R. Jones *et al.*, *Nat. Mater.* **9**, 913 (2010).
5. K. Miszta *et al.*, *Nat. Mater.* **10**, 872 (2011).
6. M. Rycenga, J. M. McLellan, Y. N. Xia, *Adv. Mater.* **20**, 2416 (2008).
7. A. Salant, E. Amitay-Sadovsky, U. Banin, *J. Am. Chem. Soc.* **128**, 10006 (2006).
8. M. L. Tang, N. Liu, J. A. Dionne, A. P. Alivisatos, *J. Am. Chem. Soc.* **133**, 13220 (2011).
9. Q. S. Wei *et al.*, *J. Am. Chem. Soc.* **131**, 9728 (2009).
10. C. T. Black, C. B. Murray, R. L. Sandstrom, S. H. Sun, *Science* **290**, 1131 (2000).
11. A. Courty, A. Mermet, P. A. Albouy, E. Duval, M. P. Pileni, *Nat. Mater.* **4**, 395 (2005).
12. J. J. Urban, D. V. Talapin, E. V. Shevchenko, C. R. Kagan, C. B. Murray, *Nat. Mater.* **6**, 115 (2007).
13. Y. Yamada *et al.*, *Nat. Chem.* **3**, 372 (2011).
14. J. Q. Zhuang *et al.*, *J. Am. Chem. Soc.* **131**, 6084 (2009).
15. L. Carbone *et al.*, *Nano Lett.* **7**, 2942 (2007).
16. D. V. Talapin *et al.*, *Nano Lett.* **7**, 2951 (2007).
17. See supplementary materials on *Science* Online.
18. J. Q. Zhuang, H. M. Wu, Y. G. Yang, Y. C. Cao, *Angew. Chem. Int. Ed.* **47**, 2208 (2008).
19. D. B. Williams, C. B. Carter, *Transmission Electron Microscopy: A Textbook for Materials Science* (Springer, New York, ed. 2, 2009).
20. L. D. Marks, D. J. Smith, *Nature* **303**, 316 (1983).
21. L. D. Marks, *J. Cryst. Growth* **61**, 556 (1983).
22. Y. Nagaoka, T. Wang, J. Lynch, D. LaMontagne, Y. C. Cao, *Small* **8**, 843 (2012).
23. P. Ball, *The Self-Made Tapestry: Pattern Formation in Nature* (Oxford Univ. Press, Oxford, 2000).
24. Y. N. Xia, Y. D. Yin, Y. Lu, J. McLellan, *Adv. Funct. Mater.* **13**, 907 (2003).
25. D. V. Talapin *et al.*, *Nano Lett.* **3**, 1677 (2003).
26. A. Sitt, A. Salant, G. Menagen, U. Banin, *Nano Lett.* **11**, 2054 (2011).
27. J. F. Wang, M. S. Gudiksen, X. F. Duan, Y. Cui, C. M. Lieber, *Science* **293**, 1455 (2001).
28. S. Y. Wang *et al.*, *Nat. Commun.* **2**, 364 (2011).

Acknowledgments: Supported by Office of Naval Research grant N00014-09-1-0441 (Y.C.C.), NSF Career Award DMR-0645520, and the Cornell High Energy Synchrotron Source through NSF award DMR-0936384. We thank S. Zou for helpful discussions and X. Liu for providing line-patterned Si_3N_4 substrates. Transmission electron microscope work was conducted at the Major Analytical Instrumentation Center at the University of Florida. A PCT International Patent Application has been filed (docket no. 995XC1PCT, "Laterally Aligned Colloidal Nanorods Assemblies," serial no. PCT/US2012/042958).

Supplementary Materials

www.sciencemag.org/cgi/content/full/338/6105/358/DC1
Materials and Methods
Supplementary Text
Figs. S1 to S27
Table S1
References (*29*–*32*)

3 May 2012; accepted 6 September 2012
10.1126/science.1224221

Integrated Compact Optical Vortex Beam Emitters

Xinlun Cai,[1] Jianwei Wang,[2] Michael J. Strain,[3] Benjamin Johnson-Morris,[1] Jiangbo Zhu,[4,5] Marc Sorel,[3] Jeremy L. O'Brien,[2] Mark G. Thompson,[2] Siyuan Yu[1,4]*

Emerging applications based on optical beams carrying orbital angular momentum (OAM) will probably require photonic integrated devices and circuits for miniaturization, improved performance, and enhanced functionality. We demonstrate silicon-integrated optical vortex emitters, using angular gratings to extract light confined in whispering gallery modes with high OAM into free-space beams with well-controlled amounts of OAM. The smallest device has a radius of 3.9 micrometers. Experimental characterization confirms the theoretical prediction that the emitted beams carry exactly defined and adjustable OAM. Fabrication of integrated arrays and demonstration of simultaneous emission of multiple identical optical vortices provide the potential for large-scale integration of optical vortex emitters on complementary metal-oxide–semiconductor compatible silicon chips for wide-ranging applications.

The discovery that photons in optical vortices—light beams with helical phase fronts and an azimuthal component of the wave vector—can carry orbital angular momentum (OAM) (*1*) may lead to wide-ranging applications in optical microscopy (*2*), micromanipulation (*3*), free-space communication (*4*, *5*), and quantum information (*6*, *7*). Techniques for generating optical vortices involve passing free-space light beams through optical elements, including computer-generated holograms (*4*, *8*), spiral phase plates (*9*), inhomogeneous birefringent elements (*10*), subwavelength gratings (*11*), and nanoantennas (*12*).

Photonic integration has been a major propellant for widespread application of photonic technologies due to advantages in reliability, miniaturization, and scalability compared with bulk optics (*13*). Compact, robust, and efficient planar waveguide–based OAM emitters and receivers are critical elements, as they can be integrated in large numbers and interconnected via waveguides with each other and with lasers and detectors to form photonic integrated circuits (PICs). Recently, a waveguide-based device has been reported for multiplexing and demultiplexing of OAM beams as a means of realizing multichannel optical communication (*5*, *14*). However, its large size (2.5 by 1.5 mm^2) and phase-sensitive arrayed waveguide structure do not yet support large-scale integration. Here, we report micrometer-sized silicon photonic waveguide OAM devices

---

[1] Photonics Group, Merchant Venturers School of Engineering, University of Bristol, Bristol, UK. [2] Centre for Quantum Photonics, University of Bristol, Bristol, UK. [3] Department of Electronics and Electrical Engineering, University of Glasgow, UK. [4] State Key Laboratory of Optoelectronic Materials and Technologies and School of Physics and Engineering, Sun Yat-sen University, Guangzhou, China. [5] State Key Laboratory of Application-Specific Integrated Circuits and Systems and Department of Communication Science and Engineering, Fudan University, Shanghai, China.

*To whom correspondence should be addressed. E-mail: s.yu@bristol.ac.uk

that emit vector optical vortices carrying well-defined, quantized, and tunable OAM, as well as integrated OAM emitter arrays that emit multiple optical vortices simultaneously.

Circular optical resonators, such as microrings or microdisks (*15*), support whispering gallery modes (WGMs) carrying high OAM (*16*, *17*). To extract the confined WGMs into free-space emission, we embed angular grating structures into the WGM resonator (Fig. 1A) with a periodic modulation of refractive index in the azimuthal direction.

The working principle of the angular grating is analogous to that of second-order gratings widely used in straight waveguides as input/output couplers (*18*), in which the guided wave is scattered by the grating elements collectively and an appreciable fraction of power is diverted in a certain direction φ, in which constructive interference occurs. The wavefront of the radiated light is a plane tilted at angle φ (Fig. 1B). If the waveguide with grating is curved to form a loop so that the guided wave forms WGMs, by way of Huygens' Principle, the wavefront of the radiated light should skew in the azimuthal direction and transform into a helix, suggesting the creation of an OAM-carrying beam (Fig. 1C). Rigorous theoretical derivation shows that a WGM only emits into a free-space beam when the following angular phase-matching condition is satisfied (*16*)

$$\nu_{\rm rad} = p - q \qquad (1)$$

where p is the azimuthal order of the WGM involved, or the number of optical periods around the resonator, and q is the number of grating elements around the resonator. $\nu_{\rm rad}$ is the azimuthal propagation constant (phase shift per unit azimuthal angle) of the radiated beam, which gives rise to the azimuthal component of the wave vector and, hence, OAM. The z component of the propagation constant of the radiation mode is given by $\beta_{{\rm rad},z} = \sqrt{(2\pi/_{\lambda})^2 - (\nu_{\rm rad}R)^2}$, where λ is the vacuum wavelength and R is the resonator radius (Fig. 1A).

Because the state of polarization (SOP) of the source WGMs and the angular grating structure are both cylindrically symmetric, the radiated beams should maintain this symmetry and should be cylindrical vector (CV) beams (*19*). In our devices (Fig. 1A), for quasi–transverse electric (TE) WGMs, the radiated near field is predominantly azimuthally polarized (*16*) with its Jones vector $E_{\rm CV}$ written as (*20*, *21*)

$$\begin{aligned} E_{\rm CV} &= \begin{pmatrix} -\sin\theta \\ \cos\theta \end{pmatrix} \exp(i\nu_{\rm rad}\theta) \\ &= \begin{pmatrix} -\sin\theta \\ \cos\theta \end{pmatrix} \exp[i(p-q)\theta] \\ &= \begin{pmatrix} -\sin\theta \\ \cos\theta \end{pmatrix} \exp(il\theta) \qquad (2) \end{aligned}$$

where θ is the azimuthal angle, and i is the unit imaginary number (Fig. 1A). Following the concept introduced in (*20*), we conclude that the radiated beams are vector vortices with a topological Pancharatnam charge of $l = p - q$. The topological Pancharatnam charge, similar to the topological charge in scalar vortices, is directly related to the OAM of vector vortices: The amount of OAM carried by the radiated beam is $l\hbar$ per photon, where $\hbar$ is Planck's constant h divided by 2π.

We therefore have a very simple yet robust OAM emitter scheme, in which l can only take integer values, being solely determined by the difference between integers p and q. Equation 1 indicates that the angular grating diffracts the light confined in a pth order WGM [carrying a OAM of $p\hbar$ per photon (*16*)] into a free-space beam, changing the OAM by an amount of $q\hbar$ per photon in the process. For a fabricated device, q is a structural constant, whereas the value of p can be changed by exciting selected WGMs. Hence, variable OAM can be generated by tuning the injected laser wavelength to various cavity resonances or, alternatively, by tuning cavity resonances with respect to a fixed injection wavelength by changing the cavity refractive index. The integer p can also take negative values corresponding to the opposite WGM propagating direction.

We designed and fabricated two types of microring devices ($R = 3.9$ μm, $q = 36$ and $R = 7.5$ μm, $q = 72$) on the same silicon-on-insulator chip (*16*), with their resonance associated with $l = 0$ to be near the center of our tunable laser's wavelength range (1470 to 1580 nm). Figure 1, D and E, shows scanning electron microscopy (SEM) images of the device with $R = 3.9$ μm.

Both types of devices have been characterized by launching continuous-wave light from a tunable laser into the access waveguide to excite the quasi-TE mode. The near-field intensity of the radiated beam from the devices, with $l = 0$, is annular with a dark center, as imaged on an infrared camera (Fig. 2A), and is predominantly azimuthally polarized (Fig. 2, B to E).

The emission spectrum of the device with $R = 7.5$ μm and $q = 72$ is shown in Fig. 3A. Each resonance corresponds to a distinctive WGM (p value). The emission efficiencies at various resonances are measured to be 3 to 13% (*16*) and are higher at the longer wavelength side due to the wavelength-dependent coupling between the access waveguide and the resonator.

We used an interference scheme to characterize the wavefront structure. We observe that the radiated CV vortex beam can be described as the superposition of two orthogonal scalar vortices, as $E_{\rm CV}$ in Eq. 2 can be further decomposed into (*22*)

$$\begin{aligned} E_{\rm CV} = \frac{i}{2}\begin{pmatrix} 1 \\ -i \end{pmatrix} \exp[i(l+1)\theta] - \frac{i}{2}\begin{pmatrix} 1 \\ i \end{pmatrix} \\ \times \exp[i(l-1)\theta] \qquad (3) \end{aligned}$$

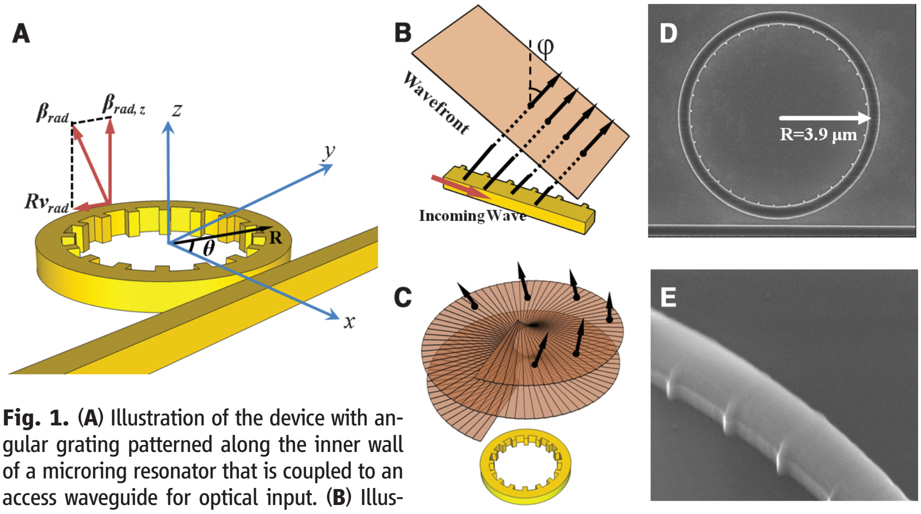

Fig. 1. (**A**) Illustration of the device with angular grating patterned along the inner wall of a microring resonator that is coupled to an access waveguide for optical input. (**B**) Illustration of a linear waveguide with gratings and the tilted wavefront of the radiated light. (**C**) Illustration of an angular grating together with the helical wavefront of the radiated beam. (**D** and **E**) SEM images of a fabricated device (R = 3.9 μm).

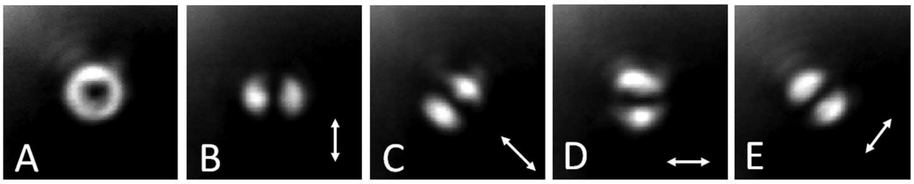

Fig. 2. (**A**) Measured near-field intensity distribution of the radiated beam with l = 0. (**B** to **E**) Measured intensity distributions after a polarizer in the directions indicated by the arrows. A two-lobe intensity pattern arranged orthogonal to the polarizer axis is obtained. When the polarizer is rotated, the two-lobe pattern rotates in the same manner, confirming that the radiated beam is a CV beam with azimuthal polarization.

which consists of a right-hand circularly polarized (RHCP) beam with topological charge of $l + 1$ and a left-hand circularly polarized (LHCP) beam with $l - 1$. This indicates a new scheme of measuring the value of l: When the radiated beam interferes with a copropagating circularly polarized reference beam, spiral interference patterns should be produced, with the number of arms equal to either $l - 1$ or $l + 1$, depending on the handedness of the reference beam SOP.

The measured interference patterns (Fig. 3, B and C) have spiral arms equal to $l - 1$ (RHCP) or $l + 1$ (LHCP) as predicted in the aforementioned scheme, and the sign of the topological charge is indicated by the chirality of the pattern. Thus, the nine resonances correspond to $l = 0, \pm1, \pm2, \pm3$, and ±4. Similar results for the device with $R = 3.9$ μm are given in the supplementary materials (*16*). Moreover, the spiral patterns rotate when the phase of the reference beam is changed continuously (movies S1 and S2). These results show unambiguously that the wavefront of the radiated beams is helical with $l = p - q$. Beams with larger OAM quantum numbers l can be generated from the device. However, the observable l is limited by the tuning range of the tunable laser.

To demonstrate the potential of photonic integration, we fabricated OAM emitter arrays consisting of three identical emitters ($R = 7.5$ μm, $q = 72$) coupled to the same access waveguide (Fig. 4, A and B). Simultaneous emission of identical vortices has been verified, as shown in Fig. 4, C and D. The spiral patterns rotate synchronously when the phase of the reference beam is changed (movie S3).

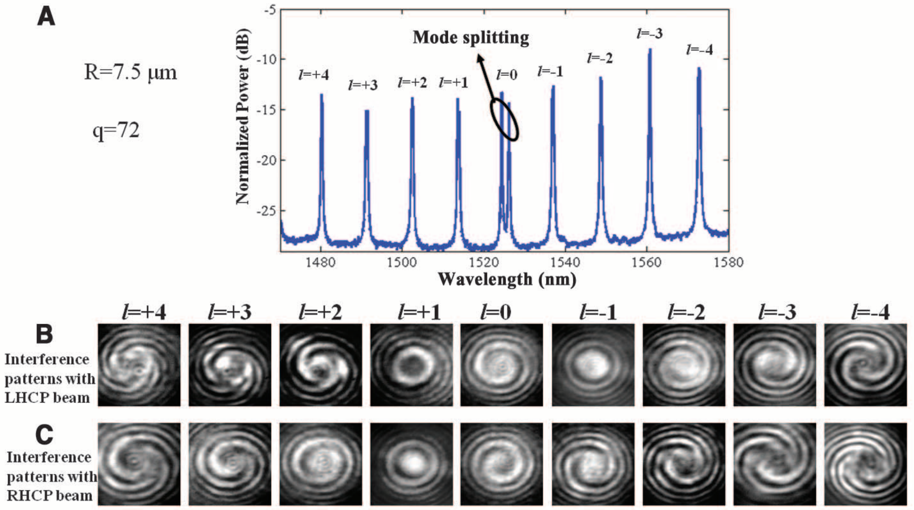

Fig. 3. (**A**) Radiation spectrum for a device with $R = 7.5$ μm measured by scanning input laser wavelength. The $l = 0$ wavelength is ~1525 nm. The doublets in the spectrum result from the mode splitting caused by cross-coupling between the otherwise degenerate clockwise and counterclockwise WGMs. The strongest cross-coupling occurs at the wavelength with $l = 0$ due to Bragg reflection, which is therefore associated with the largest split. (**B** and **C**) Interference patterns with LHCP and RHCP reference beams. Each pattern in (B) has $l + 1$ spiral arms, whereas each pattern in (C) has $l - 1$ spiral arms.

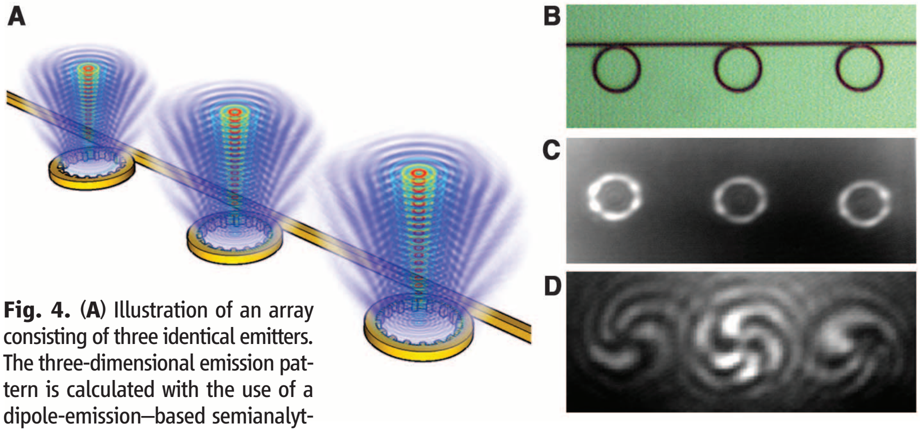

Fig. 4. (**A**) Illustration of an array consisting of three identical emitters. The three-dimensional emission pattern is calculated with the use of a dipole-emission–based semianalytical model (*16*). (**B**) Micrograph of a fabricated array. (**C**) Near-field intensity patterns emitted from the array. The difference in their brightness is attributed to slight differences in their resonance peaks due to fabrication variations. (**D**) Example of an interference pattern between the emitted beams from the array and the copropagating RHCP Gaussian beam. All beams have four arms and, therefore, the same OAM order $l = -3$. The uneven brightness is due to the Gaussian distribution of the reference beam, which is only coaxial with the middle vortex. The two side vortices are somewhat deformed due to lens aberration causing phase-front distortion.

Our OAM emitters based on complementary metal oxide semiconductor compatible silicon PICs produce optical vortex beams with distinctive and variable OAM values from a very simple and small device, with no need for any fine adjustment of optical phase. While we have already achieved useful emission efficiency of up to 13%, efficiency can be maximized by engineering the coupling ratio between the resonator and the access waveguide to the critical coupling point (*23*), at which all of the input power enters the resonator. As demonstrated by the integrated arrays, integration of a large number of devices can be realized with the use of standard integrated circuit technology to form complicated formations on silicon wafers.

Such scalable integration could open up truly large-scale integrated applications opportunities. For example, it is possible to build OAM quantum communications channels between two chips, each containing the same integrated OAM PICs—one as the OAM transmitter and the other as the OAM receiver (according to the principle of reciprocity, the device emitting a specific vortex beam will selectively receive the same beam). Though it has been shown that OAM multiplexing and demultiplexing can be achieved with the use of PICs (*14*), our device enables rapid switching among OAM states, as semiconductor tunable lasers can already switch wavelengths in nanoseconds (*24*), and silicon microrings have been shown to tune at frequencies up to 40 GHz (*25*). Therefore, our device provides an approach for an integrated OAM switch or modulator. Another application area could be micromanipulation of particles (*26*). By selectively lighting groups of integrated emitter arrays, controllable and reconfigurable drivers can be configured for microfluidic and nanoparticle manipulation machines, such as lab-on-a-chip, optical tweezers, and optical spanners.

References and Notes

1. L. Allen, M. W. Beijersbergen, R. J. C. Spreeuw, J. P. Woerdman, *Phys. Rev. A* **45**, 8185 (1992).
2. S. Fürhapter, A. Jesacher, S. Bernet, M. Ritsch-Marte, *Opt. Lett.* **30**, 1953 (2005).
3. D. G. Grier, *Nature* **424**, 810 (2003).
4. G. Gibson *et al.*, *Opt. Express* **12**, 5448 (2004).
5. N. K. Fontaine, C. R. Doerr, L. Buhl, in *Optical Fiber Communication Conference*, *OSA Technical Digest* (Optical Society of America, Washington, DC, 2012), paper OTu1I.2.
6. A. Mair, A. Vaziri, G. Weihs, A. Zeilinger, *Nature* **412**, 313 (2001).
7. G. Molina-Terriza, J. P. Torres, L. Torner, *Nat. Phys.* **3**, 305 (2007).
8. N. R. Heckenberg, R. McDuff, C. P. Smith, A. G. White, *Opt. Lett.* **17**, 221 (1992).
9. M. W. Beijersbergen, R. P. C. Coerwinkel, M. Kristensen, J. P. Woerdman, *Opt. Commun.* **112**, 321 (1994).

10. L. Marrucci, C. Manzo, D. Paparo, *Phys. Rev. Lett.* **96**, 163905 (2006).
11. G. Biener, A. Niv, V. Kleiner, E. Hasman, *Opt. Lett.* **27**, 1875 (2002).
12. N. Yu *et al.*, *Science* **334**, 333 (2011).
13. M. Smit, J. van der Tol, M. Hill, *Laser Photon. Rev.* **6**, 1 (2012).
14. C. R. Doerr, L. L. Buhl, *Opt. Lett.* **36**, 1209 (2011).
15. K. J. Vahala, *Nature* **424**, 839 (2003).
16. Materials and methods are available as supplementary materials on *Science* Online.
17. A. B. Matsko, A. A. Savchenkov, D. Strekalov, L. Maleki, *Phys. Rev. Lett.* **95**, 143904 (2005).
18. D. Taillaert *et al.*, *Jpn. J. Appl. Phys.* **45**, 6071 (2006).
19. R. Dorn, S. Quabis, G. Leuchs, *Phys. Rev. Lett.* **91**, 233901 (2003).
20. Z. Bomzon, V. Kleiner, E. Hasman, *Opt. Lett.* **26**, 1424 (2001).
21. A. Niv, G. Biener, V. Kleiner, E. Hasman, *Opt. Express* **14**, 4208 (2006).
22. I. Moreno, J. A. Davis, I. Ruiz, D. M. Cottrell, *Opt. Express* **18**, 7173 (2010).
23. A. Yariv, *Electron. Lett.* **36**, 321 (2000).
24. Y. Yu, R. O'Dowd, *IEEE Photon. Technol. Lett.* **14**, 1397 (1992).
25. S. Manipatruni, Q. Xu, M. Lipson, *Opt. Express* **15**, 13035 (2007).
26. K. Ladavac, D. Grier, *Opt. Express* **12**, 1144 (2004).

Acknowledgments: We thank M. Berry and M. Dennis (Department of Physics, University of Bristol, UK), S. Barnett (Department of Physics, University of Strathclyde, UK), and M. Padgett (Department of Physics, University of Glasgow, UK) for very useful discussions and C. Railton (Merchant Venturers School of Engineering, University of Bristol, UK) for providing the finite-difference time-domain simulation tool. J.W. is funded by European Union FP7 FET-OPEN project PHORBITEC.

Supplementary Materials
www.sciencemag.org/cgi/content/full/338/6105/363/DC1
Materials and Methods
Supplementary Text
Figs. S1 to S7
References (*27–31*)
Movies S1 to S4

25 June 2012; accepted 10 September 2012
10.1126/science.1226528

Lethally Hot Temperatures During the Early Triassic Greenhouse

Yadong Sun,[1,2]* Michael M. Joachimski,[3] Paul B. Wignall,[2] Chunbo Yan,[1] Yanlong Chen,[4] Haishui Jiang,[1] Lina Wang,[1] Xulong Lai[1]

Global warming is widely regarded to have played a contributing role in numerous past biotic crises. Here, we show that the end-Permian mass extinction coincided with a rapid temperature rise to exceptionally high values in the Early Triassic that were inimical to life in equatorial latitudes and suppressed ecosystem recovery. This was manifested in the loss of calcareous algae, the near-absence of fish in equatorial Tethys, and the dominance of small taxa of invertebrates during the thermal maxima. High temperatures drove most Early Triassic plants and animals out of equatorial terrestrial ecosystems and probably were a major cause of the end-Smithian crisis.

Anthropogenic global warming likely is contributing to the rapid loss of biological diversity currently occurring (*1*). Climate warming also has been implicated in severe biotic crises in the geological past, but only as a corollary to more direct causes of death such as the spread of marine anoxia (*2*). Here, we show that lethally hot temperatures exerted a direct control on extinction and recovery during and in the aftermath of the end-Permian mass extinction. As well as the scale of the losses, the aftermath of this event is remarkable for several reasons, such as the prolonged delay in recovery (*3*), the prevalence of small taxa (*4*), and the absence of coal deposits throughout the Early Triassic (*5*). These and several facets of low-latitude fossil records shown below, including fish, marine reptile, and tetrapod distributions, can be related to extreme temperatures in excess of tolerable thermal thresholds.

Climate warming long has been implicated as one cause of the end-Permian crisis (*2*, *6*), with carbon dioxide release from Siberian eruptions and related processes providing a potential trigger for it (*7*, *8*). Conodont apatite oxygen isotope

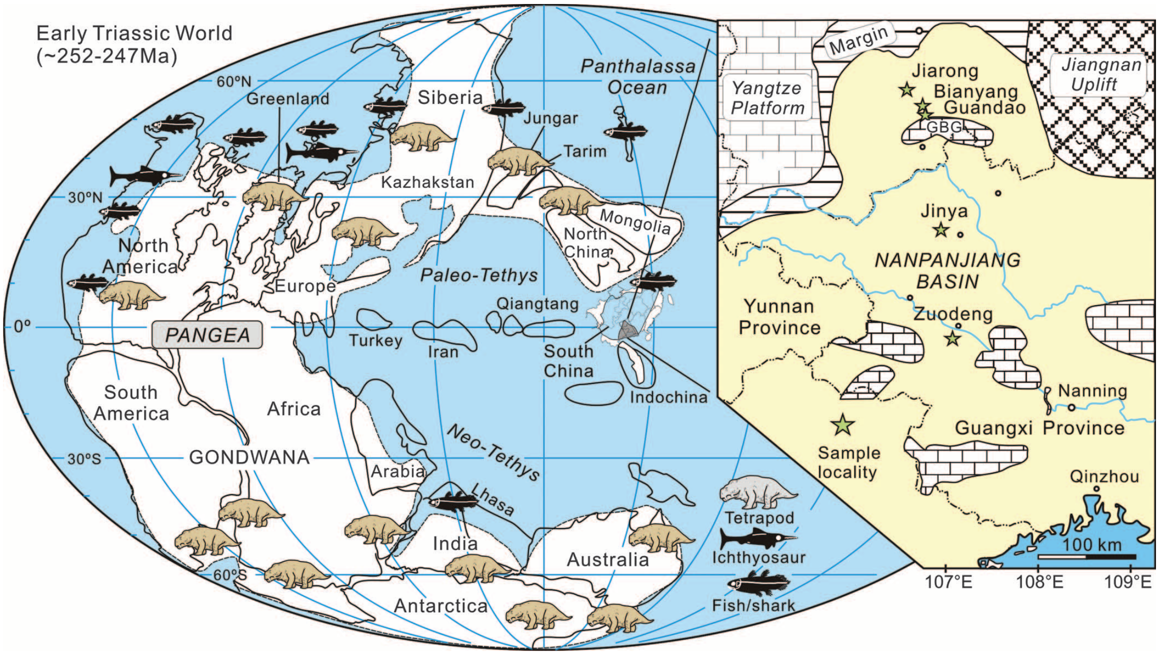

Fig. 1. Early Triassic paleogeography showing reported occurrences of fish and marine reptiles in the Smithian. Note rare equatorial occurrence of both groups when ichthyosaurs had evolved in northern climes. The global distribution of tetrapods (*25*) indicates occurrences almost exclusively in higher latitudes (>30°N and >40°S) throughout the Early Triassic, with rare exceptions in Utah (*Parotosuchus* sp., paleolatitude ~10°N) and Poland (paleolatitude ~20°N), both probably of middle-late Spathian age (*25*, *26*). (**Inset**) Paleogeography of Pangea and Nanpanjiang Basin after (*45–47*). Fish and ichthyosaurs occurrences, see table S2. GBG, Great Bank of Guizhou.

---

[1] State Key Laboratory of Geobiology and Environmental Geology, China University of Geosciences (Wuhan), Wuhan 430074, People's Republic of China. [2] School of Earth and Environment, University of Leeds, Leeds LS2 9JT, UK. [3] GeoZentrum Nordbayern, Universität Erlangen-Nürnberg, Schlossgarten 5, 91054 Erlangen, Germany. [4] Institute of Earth Sciences–Geology and Paleontology, University of Graz, Heinrichstrasse 26, A-8010 Graz, Austria.

*To whom correspondence should be addressed. E-mail: eeys@leeds.ac.uk